Pressure-induced spin collapse of octahedrally coordinated Mn^{3+} in the tetragonal hydrogarnet henritermierite $Ca_3Mn_2[SiO_4]_2[O_4H_4]$

Alexandra Friedrich,* Björn Winkler, and Wolfgang Morgenroth
Institut für Geowissenschaften, Goethe-Universität, Altenhöferallee 1, D-60438 Frankfurt a.M., Germany

Alexander Perlov and Victor Milman
Dassault Systèmes BIOVIA, 334 Science Park, Cambridge CB4 0WN, England, United Kingdom
(Received 22 January 2015; revised manuscript received 11 May 2015; published 29 July 2015)

The high-pressure behavior of natural henritermierite garnet with close to end-member composition $Ca_3Mn_2[SiO_4]_2[O_4H_4]$ was studied at pressures up to 80 GPa using single-crystal synchrotron x-ray diffraction, Raman spectroscopy, and quantum-mechanical calculations based on density functional theory. An isosymmetric phase transition was observed in the pressure range between 55 and 70 GPa, which is associated with a gradual high-spin to low-spin electronic transition in Mn^{3+} and a pronounced reduction of the Jahn-Teller distortion of the $Mn^{3+}O_4(OH)_2$ octahedra. In the high-pressure phase the Jahn-Teller distortion is totally suppressed and the Mn^{3+} is in a low-spin configuration. Experimental structural data before and after the phase transition are in excellent agreement with the theoretically predicted structural compression of the high-spin and low-spin phases, respectively. While the overall unit-cell volume is reduced by about 1.5% across the phase transition, a collapse of about 4–5% of the MnO_6 octahedral volume is observed. The high-spin phase shows a bulk modulus B = 101(1) GPa and its pressure derivative $B' = 4.5(1)$. The bulk moduli of the coordination polyhedra are B_{MnO_6} = 178(2) GPa, $B_{Ca1O_8} = 101.2(5)$ GPa, $B_{Ca2O_8} = 88.4(8)$ GPa, $B_{SiO_4} = 337(5)$ GPa, and $B_{O_4H_4} = 29(1)$ GPa for the high-spin phase. Mode Grüneisen parameters range between 0.34 and 0.94. The computed spin-pairing energy is ≈3.6 eV at 0 GPa.

DOI: 10.1103/PhysRevB.92.014117 PACS number(s): 61.50.Ks, 61.05.cp, 71.15.Mb, 78.30.−j

I. INTRODUCTION

Pressure-induced spin transitions have already been predicted by Fyfe [1], and high-pressure experiments allowed one to obtain the first experimental evidence for these electronic transitions in $Fe_{0.94}O$ [2], Fe_2O_3 (hematite) [3,4], and FeS [5] using Mössbauer spectroscopy and x-ray-emission spectroscopy. While a large number of studies have already been published on spin transitions in ferric or ferrous oxides, spin-pairing transitions have rarely been studied in manganese-bearing inorganic compounds. Due to its electronic structure (d^4 configuration), the Mn^{3+} ion may undergo a spin-pairing transition from the high-spin (HS) ($S = 2\ \hbar$) to the low-spin (LS) ($S = 1\ \hbar$) state at high pressure. There exists no intermediate spin state for the d^4 configuration. A pressure-induced spin change in Mn^{3+} was reported in $CsMnF_4$ at 37 GPa based on optical absorption spectroscopy, where, concomitantly with the spin transition, the suppression of the Jahn-Teller distortion of the MnF_6 octahedron was observed [6]. Due to the electronic configuration it is expected that low-spin Mn^{3+} does not induce a Jahn-Teller distortion in an octahedral configuration. In the present study we report on a pressure-induced spin transition of Mn^{3+} in octahedral oxygen coordination in henritermierite, which is a Mn^{3+}-bearing hydrogarnet with the end-member formula $Ca_3Mn_2[SiO_4]_2[O_4H_4]$ [7,8], from single-crystal x-ray diffraction (XRD), Raman spectroscopy, and quantum-mechanical calculations based on density functional theory (DFT). The influence of Mn^{3+}/Fe^{3+} and SiO_4/O_4H_4 substitution on the spin transition and the pressure evolution of the Jahn-Teller distortion of the MnO_6 octahedra will be discussed.

Recently, we have described a pressure-induced spin transition in Fe^{3+} in the silicate garnet andradite, $Ca_3Fe_2[SiO_4]_3$, at pressures of 60–70 GPa [9]. A substitution of Mn^{3+} for Fe^{3+} within the garnet group allows us to investigate whether octahedrally coordinated Mn^{3+} shows a high-spin to low-spin (HS-LS) transition at similarly high pressures. In the Mn^{3+}-bearing garnets $Ca_3Mn_2[SiO_4]_3$ and $Mn_3^{2+}Mn_2^{3+}[SiO_4]_3$ (blythite) the Jahn-Teller distortion of the $Mn^{3+}O_6$ octahedra is disordered and hence its magnitude cannot be extracted from x-ray-diffraction data in detail [10,11]. However, in henritermierite the Jahn-Teller distortion of the $Mn^{3+}O_4(OH)_2$ octahedra ("$Mn^{3+}O_6$ octahedra" in the following) is ordered. Hence, henritermierite is an ideal compound to study both the spin transition in Mn^{3+} and the evolution of the Jahn-Teller distortion of the $Mn^{3+}O_6$ octahedra at high pressure using x-ray diffraction.

Unlike the majority of garnets, which are cubic and crystallize in space group $Ia\bar{3}d$, henritermierite is tetragonal (space group $I4_1/acd$) [7,8]. This is due to the ordered arrangement of small SiO_4 and large O_4H_4 tetrahedra and the Jahn-Teller distortion of octahedrally coordinated Mn^{3+} (Fig. 1). The crystal structure and hydrogen bond geometry were investigated by diffraction, optical, and spectroscopic (UV-VIS and IR) methods in detail [8,12]. The hydrogen atoms form intratetrahedral bifurcated hydrogen bonds and interpolyhedral hydrogen bonds with the O2 atoms, which are part of the elongated Mn–O2 axes of the Jahn-Teller distorted MnO_6 octahedra (Fig. 2). It was argued by Armbruster *et al.* [8] that 1/3 of the oxygen atoms in henritermierite form weak Mn–O bonds (Mn–O2) and due to underbonding are preferred to accept an additional hydrogen bond, which is the reason for the stoichiometry with a $[SiO_4]/[O_4H_4]$ ratio of 2:1 and an ordered arrangement of the O_4H_4 tetrahedra within the

*friedrich@kristall.uni-frankfurt.de

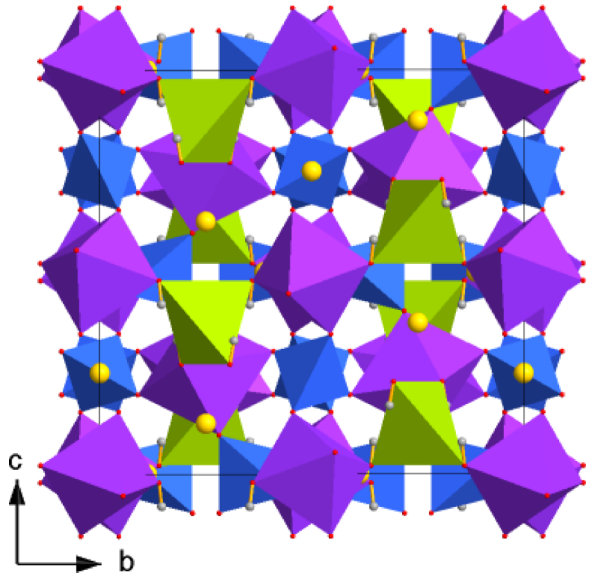

FIG. 1. (Color online) Crystal structure of henritermierite. MnO_6 octahedra (purple), SiO_4 tetrahedra (small, blue), and O_4H_4 tetrahedra (large, green) share corners in a three-dimensional framework. Ca atoms (yellow spheres) occupy triangular dodecahedral sites with eightfold coordination. O–H bonds are shown for the O_4H_4 tetrahedra.

crystal structure. There are two symmetrically independent CaO_8 polyhedra. The Ca2 atom occupies a symmetrically fully constrained position (0 1/4 1/8) in henritermierite, similar to that of the Ca atom in andradite. The Ca1 atom is slightly displaced along the *a* axis and occupies a less symmetric position with a twofold site symmetry. The $Ca1O_8$ polyhedron displays a quite regular coordination, while the $Ca2O_8$ polyhedron is significantly distorted, forming four short and four long Ca–O distances. The distortion of the $Ca2O_8$ polyhedron is stronger in henritermierite than in andradite. No Raman-spectroscopic measurements of the vibrational properties have been published so far. Single-crystal x-ray diffraction at pressures up to 8.7 GPa showed a reduction

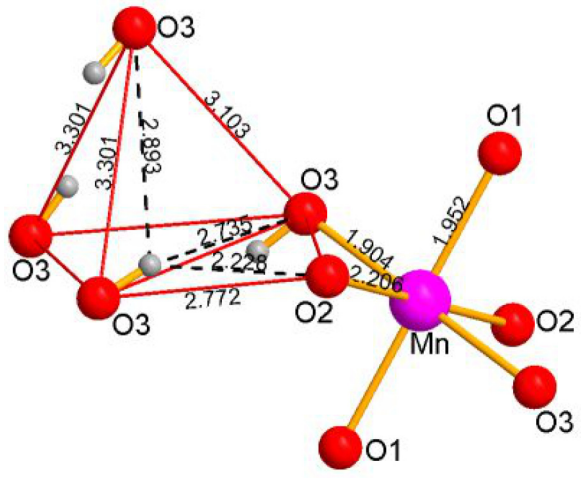

FIG. 2. (Color online) Bonding in henritermierite showing the connectivity between the O_4H_4 tetrahedron and the MnO_6 octahedron. The O2–Mn–O2 axis is Jahn-Teller elongated. Distances are given in Å.

of the Jahn-Teller distortion of the $Mn^{3+}O_6$ octahedra [8]. No pressure-induced phase transition has been detected so far [8].

Henritermierite is a member of the hydrogarnet group of minerals. Garnets are potential hosts for the storage of water in the Earth's mantle. A few studies have addressed the influence of the hydrogarnet substitution on the high-pressure behavior in the hydrogrossular series grossular $Ca_3Al_2[SiO_4]_3$-katoite $Ca_3Al_2[O_4H_4]_3$ [13,14]. A pressure-induced phase transition from space group $Ia\bar{3}d$ to $I\bar{4}3d$ was reported in katoite at above 5 GPa [13,14]. Polyhedral bulk moduli were obtained and the comparatively low bulk modulus of katoite [B_0 = 57.9(7) GPa [13]] with respect to that of grossular [B_0 = 175(1) GPa [15]] was primarily attributed to the high compressibilities of the CaO_8 dodecahedron [$B_0 = 61(2)$ GPa] and (O_4H_4) tetrahedron [$B_0 = 35(2)$ GPa] [13]. We are interested in the effect of hydrogarnet substitution on the spin transition and in the evolution of the hydrogen bond geometries across the spin transition. A correlation of the pressure-induced spin collapse in Fe^{3+} and the hydrogen bond symmetrization was reported previously in α- and ε-FeOOH [16,17], and we are interested whether such a correlation exists in henritermierite as well.

II. METHODS

A. Experimental details

The sample material comes from the N'Chwaning II mine, Kalahari manganese ore fields, Republic of South Africa, and was obtained from T. Armbruster (Bern, Switzerland) and J. Gutzmer (Freiberg, Germany). The crystal structure and chemical composition of this material have been characterized earlier and a near-to-end-member composition $(Ca_{2.98}Na_{0.01}Mg_{0.01})(Mn_{1.95}Fe_{0.01}Al_{0.04})[SiO_4]_{2.07}[O_4H_4]_{0.93}$ was reported from electron microprobe analyses [8].

Small single crystals of henritermierite (10–50-μm diameter and 5–20-μm thickness) were loaded together with ruby chips for pressure determination [18] into holes of 80–140-μm diameter in tungsten or rhenium gaskets preindented to thicknesses of 20–45 μm in Boehler-Almax diamond anvil cells equipped with conical diamonds of 200–350-μm culet diameters and 48–78° opening angles [19]. Neon was loaded at a pressure of 0.18 GPa as a pressure-transmitting medium. On pressure increase the single crystals remained optically transparent and orange colored up to the highest pressure obtained.

Single-crystal synchrotron x-ray diffraction was performed at the Extreme Conditions Beamline P02.2 at PETRA III (DESY-Photon Science, Hamburg, Germany) [20]. The synchrotron beam with a wavelength of 0.289 or 0.290 Å was focused to a spot of about 1.7 (H) × 2.6 (V) μm^2 full width at half maximum (FWHM) using Kirkpatrick-Baez mirrors or about 9 (H) × 3 (V) μm^2 FWHM using a compact refractive lens system. Diffraction images were collected on compression [except for the data from crystal no. 3, which were collected on decompression from 65.3(3) GPa] at various pressures up to 80 GPa with a PerkinElmer XRD 1621 flat-panel detector at sample-to-detector distances of 399.9–400.9 mm by 1°ω scanning across the opening angle of the cell. The image format was converted according to the procedure described by Rothkirch *et al.* [21] for further processing with the CrysAlis^{Pro} software (version 1.171.36.28) [22] for indexing Bragg reflections,

intensity data reduction, and empirical absorption correction. Crystal structures were refined with SHELXL97-2 [23], operated using the WinGX interface [24]. The final refinement was carried out with anisotropic displacement parameters for all cations and isotropic displacement parameters for the oxygen atoms. The Mn:Al ratio was refined for the octahedral site with the constraint that the sum of the occupancies of Mn and Al was fixed to 1. The silicon occupancy on the Si2 tetrahedral site was refined. The refinement of the anisotropic displacement parameters was constrained to be equal for both silicon sites. An extinction correction was applied for all crystals. The polyhedral volumes were calculated with the program IVTON [25]. See [26] for detailed tables of the experimental details, crystal data, and refinement results for the HS phase, spin transition region, and LS phase.

Micro-Raman measurements were performed with a Renishaw Raman spectrometer (RM-1000) equipped with a CCD detector and a green Nd:YAG-laser (532 nm, 200 mW). The system was calibrated using the band at 519 cm^{-1} of a silicon wafer [27]. We employed a nonconfocal geometry and a 20× objective lens with a long-working distance. The pressure was measured before and after each exposure. The samples were the same single crystals (except for crystal no. 2) as were used for the single-crystal x-ray-diffraction experiments. Raman spectra were measured on compression before diffraction experiments or on decompression afterwards. The spectra were recorded in the range from 100 to 1300 cm^{-1} at high pressures and from 100 to 4000 cm^{-1} at ambient conditions. All spectra were corrected by subtracting a background and fitted to Lorentzian functions using the program DatLab [28].

B. Computational details

The quantum-mechanical calculations were performed based on density functional theory for a pure henritermierite end-member composition, $Ca_3Mn_2^{3+}[SiO_4]_2[O_4H_4]$ using the program CASTEP [29]. The calculations were performed with the on-the-fly pseudopotentials from the CASTEP database using a kinetic cutoff energy of 610 eV and a $3 \times 3 \times 3$ Monkhorst-Pack grid for the primitive unit cell [30], yielding distances $\leqslant 0.04$ $Å^{-1}$ between sampling points of the reciprocal lattice. The PBEsol [31] exchange correlation functional and a Hubbard $U = 2.5$ eV for the Mn d electrons was employed. A value of 2.5 eV for U was chosen as a detailed analysis of the influence of U on Mn in octahedral coordination in an unpublished study on MnOOH showed that this value correctly reproduced the local distortion and compression behavior. While some studies (e.g., [32,33]) use much larger values of 5–7 eV, it seems that for most compounds a value for U between 2.5 and 3 eV is sufficient to open a direct gap (e.g., [34]). In the present study and in our unpublished work, we find that the detailed local geometry around octahedrally coordinated manganese and the compression behavior are best modelled when $U \approx 2.5$ eV. Variations in U by 10–20% have only a little influence on the interatomic distances. The use of DFT(+U) models to study pressure-induced spin transitions in minerals is well established, e.g., ferropericlase (Mg,Fe)O [35,36], magnetite Fe_3O_4 [37,38], ε-FeOOH [17], andradite $Ca_3Fe_2[SiO_4]_3$ [9], and iron in perovskite and postperovskite $MgSiO_3$ [39–41].

The high-spin (HS) and the low-spin (LS) structures represent local minima in the total energy hypersurface. Hence, we chose the corresponding formal spin states as starting values, but allowed full spin relaxation after a few self-consistent field cycles. The results were then analyzed by a Mulliken population analysis and invariably showed either the HS or LS state. The computational approach used here is better than 1% with respect to the reproduction of the volume of the ambient pressure phase. The c/a ratio of the ambient pressure structure is reproduced to within 0.3%. The interatomic distances are reproduced with a similar accuracy.

III. RESULTS

A. DFT-based computations

The ambient pressure structure obtained from the theoretical calculations based on DFT was in good agreement with experimental values (Table I). From the DFT calculations a pressure-induced HS-LS transition in Mn^{3+} was predicted in henritermierite. From the differences of the enthalpies of the HS and LS configuration the spin transition pressure was predicted to be about 58 GPa from calculations employing a Hubbard $U = 2.5$ eV for the Mn. The predicted decrease of the unit-cell volume from the HS to the LS phase is about 2.1%.

The DFT calculations converged to insulating ferromagnetic ground-state structures with a band gap of ≈1.1 eV at ambient pressure in the HS state. A population analysis for the HS phases yielded a nominal spin for each Mn^{3+} of ≈2.0 $\hbar$, in agreement with the ideal value of $4 \times \frac{1}{2}\hbar$. This value was only weakly dependent on pressure and decreased to ≈ 1.9 $\hbar$ at 40 GPa. For the LS structures, which converged to insulating ferromagnetic ground-state structures as well, the population analysis gave ≈1 $\hbar$, in agreement with the expected ideal value of $2 \times \frac{1}{2}\hbar$. Again, there was no significant pressure dependence of this spin population and no intermediate values were observed in the DFT calculations.

DFT calculations allow us to compute the spin-pairing energy (SPE). For this, we first compute the ground-state energy of a fully geometry-optimized structure. Then we fix all structural parameters and recompute the ground-state energy by a self-consistent total-energy calculation in which the ions are constrained to be in a low-spin state. The difference between these two energies (ΔE) is 1.7 eV per Mn^{3+} ion. Mn^{3+} is a d^4 ion, which in the high-spin state contributes a crystal-field stabilization energy of $-6Dq$ and in the low-spin state contributes a crystal-field stabilization energy of $-16Dq$ [42]. The energy difference between the two states we calculated is $\Delta E = -10Dq + \text{SPE}$. For henritermierite $10Dq \approx$ 1.9 eV [12], and hence SPE = 3.6 eV, which corresponds to 29 036 cm^{-1}. This is in reasonable agreement with the SPE value of 25 215 cm^{-1} for the field-free ion [42]. A similar calculation for Fe^{3+} in andradite yielded a SPE of 33 553 cm^{-1} [9], while the experimental value for a field-free ion is 29 875 cm^{-1} [42]. For both Fe^{3+} and Mn^{3+} the theoretical values are therefore ≈12–15% larger than the experimental values for the field-free ion, despite the expectation that due to the nephelauxetic effect a bond ion should have a smaller SPE than the field-free ion. However, the accuracy of DFT + U calculations of such a sensitive property as SPE is not established yet and it needs to be confirmed by experiments.

TABLE I. Overall, axial, and polyhedral bulk moduli B (given in GPa) of henritermierite. Experimental unit-cell data of this study and Armbruster *et al.* [8] up to 55.4 GPa and DFT data for the HS configuration up to 50 GPa were fitted with a third-order Birch-Murnaghan equation of state (BM-EOS). For the fit of the experimental polyhedral volumes both a second-order and a third-order BM-EOS were used, while the compression of the O_4H_4 tetrahedral volume was better described by a third-order or fourth-order BM-EOS. V_0 and M_0 are the unit-cell volume and unit-cell axis at ambient pressure, respectively; B' is the pressure derivative of B; and B'' is the pressure derivative of B'. Our fit results are compared with those from literature data up to 8.6 GPa [8].

Ref.	V_0 (Å^3) or M_0 (Å)	B	B'	B''
$p-V$ (unit cell)				
Expt. (third)	1857.6(7)	101(1)	4.5(1)	
DFT (third)	1846.2(5)	92.5(4)	5.05(3)	
Expt. [8] (third)	≈1858	97.9(9)	5.3(3)	
$p-a$ (unit cell), $M_0=a_0$				
Expt. (third)	12.488(2)	265(4)	14.6(4)	
DFT (third)	12.478(1)	230(1)	16.79(7)	
Expt. [8] (third)	≈12.49	256(2)	17.5(9)	
$p-c$ (unit cell), $M_0=c_0$				
Expt. (third)	11.907(3)	435(13)	9.6(7)	
DFT (third)	11.864(1)	405(3)	11.5(1)	
Expt. [8] (third)	≈11.911	407(5)	13.6(1.5)	
$p-V$ ($Ca1O_8$)				
Expt. (second)	24.87002(3)	101.2(5)	4	
DFT (second)	24.29(3)	109.3(9)	4	
Expt. (third)	24.87002(6)	101(5)	4.0(3)	
DFT (third)	24.399(8)	99.1(5)	4.55(3)	
$p-V$ ($Ca2O_8$)				
Expt. (second)	25.49003(5)	88.4(8)	4	
DFT (second)	25.04(4)	88.6(9)	4	
Expt. (third)	25.4900(6)	85(23)	4.3(1.9)	
DFT (third)	25.194(8)	78.9(3)	4.54(2)	
$p-V$ (MnO_6)				
Expt. (second)	10.91001(2)	178(2)	4	
DFT (second)	10.95(2)	174(3)	4	
Expt. (third)	10.91001(1)	201(7)	2.72(3)	
DFT (third)	11.017(5)	140(1)	5.96(9)	
$p-V$ (SiO_4)				
Expt. (second)	2.251(0)	337(5)	4	
DFT (second)	2.2428(6)	340(1)	4	
Expt. (third)	2.251(0)	327(19)	4.6(1.1)	
DFT (third)	2.2449(2)	322(1)	4.79(5)	
$p-V$ (O_4H_4)				
Expt. (third)	3.95801(3)	29(1)	3.30(8)	
DFT (third)	4.07(4)	21(1)	3.56(5)	
DFT (fourth)	3.96(2)	29(1)	2.6(1)	−0.085(5)

B. Single-crystal x-ray diffraction

1. *Compression behavior of the high-spin phase at pressures up to 55.4 GPa: Bulk, polyhedral, and axial compressibilities*

Our single-crystal experiments clearly indicated structural changes attributed to a HS-LS transition at pressures above 55.4 GPa. Hence, first the compression of the HS phase will be discussed in this section for pressures up to 55.4 GPa. The pressure evolution of the unit-cell volume and lattice parameters is shown in Fig. 3.

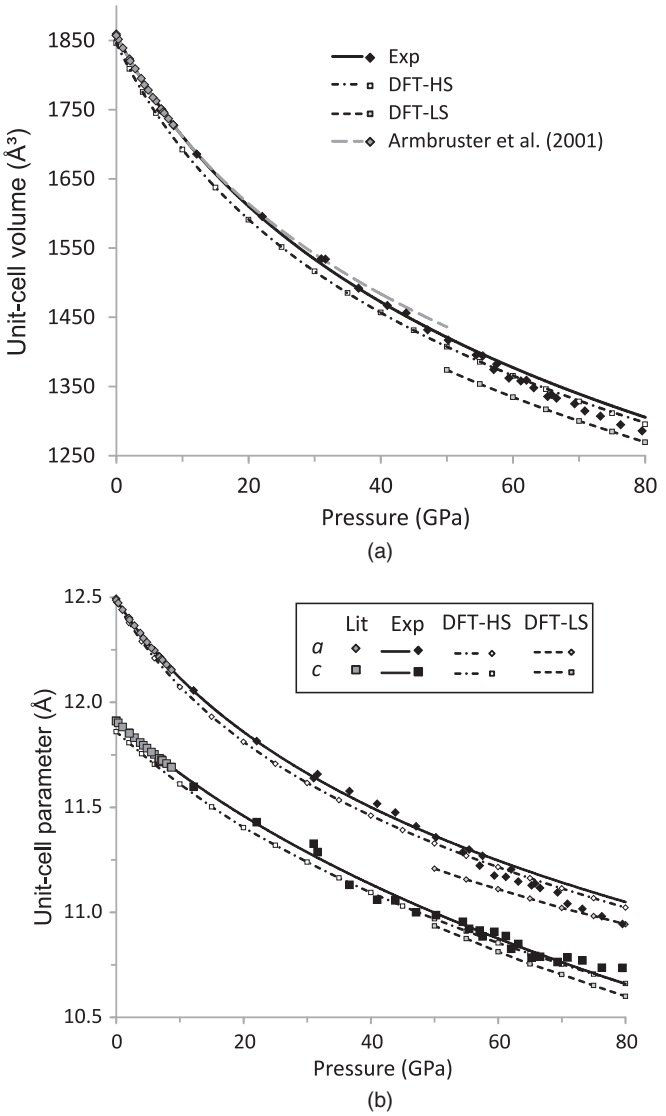

FIG. 3. Compression of the (a) unit-cell volume and (b) unit-cell parameters of henritermierite obtained from single-crystal x-ray diffraction (XRD) (Exp) and from DFT calculations for the high-spin (HS) and low-spin (LS) configurations. At pressures between 55 and 70 GPa the HS-LS crossover zone is observed. Lines represent equation of state fits to the (a) $p-V$ and (b) $p-a$ and $p-c$ data of the HS phase and guides for the LS phase. Literature values (Lit) from single-crystal XRD [8] are included in the plots and fits.

The pressure dependencies of the axial parameters, as well as the overall and polyhedral volumes of henritermierite from experiment and theory, were fitted to third- and second-order Birch-Murnaghan equations of state (BM-EOSs), respectively, using a least-squares method as implemented in the program EosFit [43]. While the large number of experimental data points and their good accuracy allowed reliable fits to third-order BM-EOSs, additional fits to second-order BM-EOSs were performed for the polyhedral volumes in order to allow a better comparison with other compounds. A fit to a

fourth-order BM-EOS was applied for the theoretical $p-V$ data of the O_4H_4 tetrahedral volume. In this case, a second-order BM-EOS could not fit both the experimental and theoretical data adequately and the third-order BM-EOS resulted in a moderate fit for the theoretical data only. In our EOS fit up to pressures of 55.4 GPa we included the data published by Armbruster *et al.* [8]. Data points were weighted with the experimental errors of both the pressures and the volumes for the axial and overall bulk moduli, while unit weights were used for the polyhedral volume data. Fits to the DFT data of the HS phase were performed in the pressure range from 0 to 50 GPa. Results are given in Table I. See [26] for a plot of the relative volume compression of the polyhedra obtained from experiments.

The experimentally determined overall bulk modulus, $B = 101(1)$ GPa, is slightly larger than a value published previously [8] (Table I). This is related to the correlation between B and B' [44]. Because in the present study more data points covering a larger pressure interval have been employed, the present results are to be preferred over the older data. The higher compressibility of the a axis compared to that of the c axis (Table I) can be attributed to the strong pressure-induced compression of the Jahn-Teller elongated axis within the MnO_6 octahedron, which is oriented close to the $[100]_{tetr}$ direction [8]. Our results clearly reflect the expected high stiffness of the SiO_4 tetrahedron, which has a bulk modulus $B_{SiO_4} = 337(5)$ GPa close to that reported for the SiO_4 tetrahedron in andradite with $B_{SiO_4} = 348(11)$ GPa [9] and typical for those of silicate garnets, which were calculated in the range $B_{SiO_4} = 327$–434 GPa using DFT [45]. However, in contrast to andradite, about one-third of the SiO_4 tetrahedra are replaced by much larger (nearly twice the volume, Fig. 4) O_4H_4 tetrahedra in henritermierite, which show a very high compressibility and $B_{O_4H_4} = 29(1)$ GPa. This value is very close to that reported for the O_4H_4 tetrahedra in katoite [$B_{O_4H_4} = 35(2)$ GPa [13]]. Due to the very different compressibilities of the SiO_4 and O_4H_4 tetrahedra their volumes become very similar at high pressures, and at pressures above 60 GPa the volume of the O_4H_4 tetrahedron is smaller than that of the much less compressible SiO_4 tetrahedron (Fig. 4). This implies that the "hydrogarnet defect" becomes increasingly stable at very high pressures.

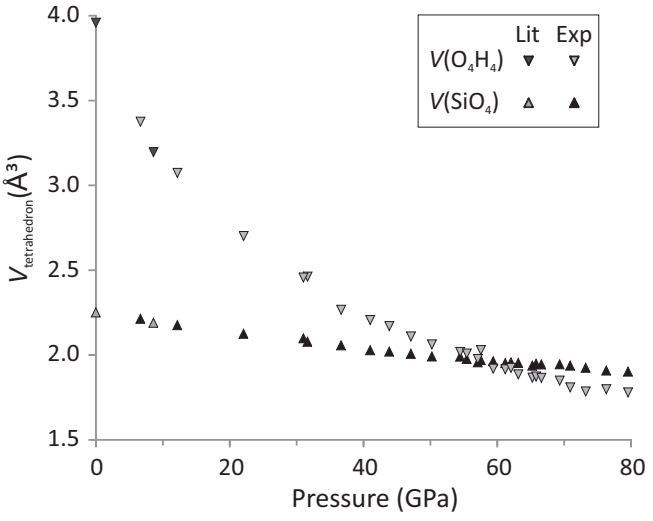

FIG. 4. Volume compression of the O_4H_4 and SiO_4 tetrahedra in henritermierite obtained from experiment and literature [8]. At about 55 GPa the large and highly compressible O_4H_4 tetrahedron is compressed to a similar volume as the small and stiff SiO_4 tetrahedron.

The $Ca2O_8$ polyhedron [$B_{Ca2O_8} = 88.4(8)$ GPa] is more compressible than both the $Ca1O_8$ polyhedron in henritermierite [$B_{Ca1O_8} = 101.2(5)$ GPa] and the CaO_8 polyhedron in andradite [$B_{CaO_8} = 104(2)$ GPa [9]]. This may be attributed to the fact that the more compressible $Ca2O_8$ dodecahedron shares two edges with the highly compressible O_4H_4 tetrahedra, while the $Ca1O_8$ polyhedron shares two edges with the incompressible SiO_4 tetrahedra similar to the CaO_8 dodecahedron in andradite. In katoite, however, the CaO_8 polyhedron is even more compressible with $B_{CaO_8} = 61(2)$ GPa [13], which was also attributed to the higher compressibility of the O_4H_4 tetrahedron compared to that of the SiO_4 tetrahedron and its pronounced effect on the compression of the longer one of the Ca–O bonds by Lager and von Dreele [46]. In summary, the different bulk moduli for different CaO_8 dodecahedra show that the bulk modulus of large polyhedra such as the CaO_8 dodecahedra, which fill the cavities of the corner-sharing tetrahedral and octahedral framework of garnets, depends not only on the respective central cation and its coordination but also on the surrounding structure and its compressibility.

2. *Spin transition*

The pressure dependencies of the unit-cell volume and the cell parameters obtained from single-crystal x-ray diffraction do not show distinct discontinuities at high pressures but only smooth changes of the compression behavior above 55 GPa (Fig. 3). A comparison with the predicted pressure evolution of the unit-cell volume and cell parameters of the HS and LS phases indicates the existence of a spin transition in Mn^{3+} with the LS phase being stable above about 70 GPa. A smaller volume drop of about 1.5% was observed experimentally compared to theory (Fig. 3). We note that powder x-ray diffraction alone would not permit the detection of a spin transition. In contrast, our single-crystal data allow us to follow the pressure evolution of the $Mn^{3+}O_6$ octahedral volume. Here, a pronounced compression is observed between 55 and 70 GPa (Fig. 5). While experimental compression data agree excellently with theoretical calculations up to about 55 GPa for the HS phase and well from 70 to 80 GPa for the LS phase, the data between 55 and 70 GPa cannot be well explained by either of the phases from theory and hence are interpreted as a spin crossover zone, where the experimental data reflects a gradual spin transition across a pressure range of about 15 GPa. The volume collapse at the spin transition is clearly more pronounced in the $Mn^{3+}O_6$ octahedra (with 4–5% decrease) than in the overall compression (Fig. 5). This shows that the phase transition observed experimentally is definitely associated with the HS-LS transition in Mn^{3+}. As the single crystals remained optically transparent and orange colored across the phase transition up to the highest pressure obtained, a transition to a metallic state can be excluded as the driving force for the octahedral volume collapse.

The phase transition is isosymmetric and reversible with no or only a small hysteresis of about 1 GPa. Slight monoclinic

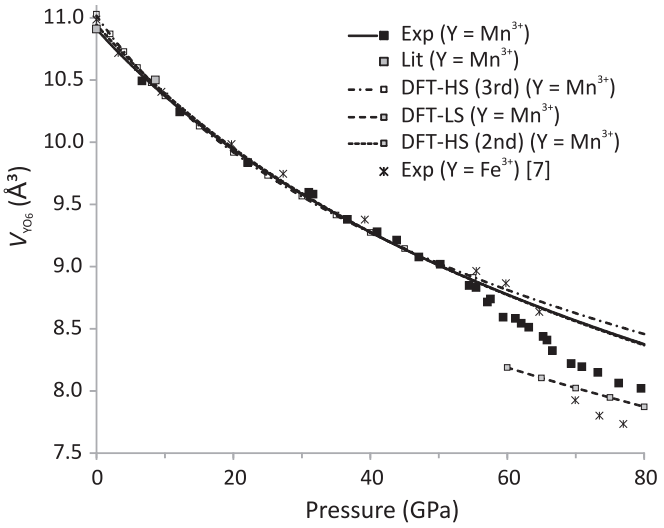

FIG. 5. Polyhedral volume compression of the MnO_6 octahedron in henritermierite obtained from experiment (Exp), literature (Lit) [8], and DFT calculations for the high-spin (HS) and low-spin (LS) configurations. An increased continuous volume drop is observed in the spin crossover zone between 55 and 70 GPa indicating a gradual spin transition. Lines represent equation of state fits to the data of the HS phase and a guide to the eye for the LS phase. Experimental data of the volume compression of the $Fe^{3+}O_6$ octahedron in andradite (stars) [9] are shown for comparison. Errors are smaller than the symbol size.

and triclinic deviations of the unit-cell parameters (up to 0.1 Å for a and b parameters and 0.6° for the angles) from tetragonal symmetry at very high pressures are attributed to slight stress effects rather than to lowering of the symmetry at the phase transition. This is supported by the facts that the extinction rules of space group $I4_1/acd$ were still obeyed and no additional reflections appeared on transition into the LS phase. Hence, the unit-cell dimensions were constrained to tetragonal symmetry at these pressures.

3. *Jahn-Teller distortion of the* MnO_6 *octahedron*

At ambient pressure, the $Mn^{3+}O_6$ octahedron has C_{2v} point-group symmetry and is Jahn-Teller elongated, forming two long apical bonds with oxygen ligands (Mn–O2 = 2.2 Å) and four shorter equatorial bonds (Fig. 6). As was already observed in the earlier study up to 8.6 GPa [8] the Jahn-Teller distortion of the octahedron is reduced on pressure increase as the two long bonds are much more compressible than the shorter ones (Fig. 6). However, a much more pronounced reduction of the Jahn-Teller distortion is observed in the spin crossover zone between 55 and 70 GPa, where the long Mn–O2 bonds are strongly compressed, while the shortest Mn–O3 bond lengths remain nearly constant. At 70 GPa and higher pressures all Mn–O distances approach to similar values and the Jahn-Teller distortion is suppressed (Fig. 6). This is another indication for the existence of the LS state of Mn^{3+}, which is not expected to show Jahn-Teller distorted octahedral coordinations.

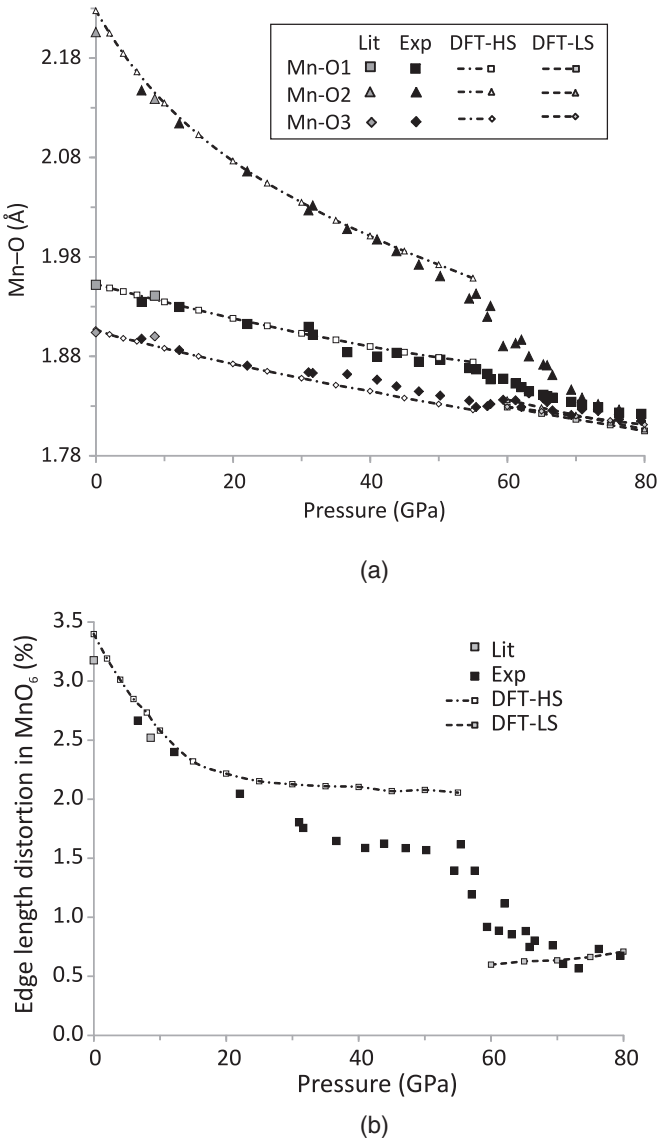

FIG. 6. (a) Compression of the Mn–O bond distances in henritermierite obtained from experiment (Exp), literature (Lit) [8], and DFT for HS and LS configurations. The Jahn-Teller distortion of the $Mn^{3+}O_6$ octahedron is reduced with pressure showing a pronounced reduction in the spin transition zone at 55–70 GPa and a complete suppression in the LS phase above 70 GPa. (b) Pressure dependence of the edge length distortion (ELD) in MnO_6. The reduction of the ELD is well reproduced by theory for the HS and LS phases. Lines are guides to the DFT-HS (dash-dotted lines) and DFT-LS (dashed lines) data.

The edge length distortion (ELD) describes the distortion of the MnO_6 octahedron and is characterized by

$$\mathrm{ELD}(\%) = \frac{100}{n}\sum_{i=1}^{n}\frac{|OO_i - \langle OO\rangle|}{\langle OO\rangle},$$

where OO_i is the edge length of the polyhedron and $\langle OO\rangle$ is the average edge length [47]. The edge length distortion of the MnO_6 octahedron decreases with pressure up to about 35 GPa and then remains constant on further pressure increase, before it strongly decreases between 55 and 70 GPa across the spin transition zone (Fig. 6). This might be attributed to the

successive decrease of the orientationally ordered Jahn-Teller distortion.

4. Bond compression

The bond distances in the SiO_4 tetrahedron and CaO_8 triangular dodecahedra show only slight but distinct anomalies across the spin transition, which are excellently reproduced by theory for the HS and LS states. The two Si–O bond lengths become similar on compression. Two edge lengths (O3 · · · O3) are distinguished in the O_4H_4 tetrahedron and become similar on compression as well. See [26] for figures of the compression of the Si–O bonds and O3 · · · O3 edge lengths. The significantly distorted $Ca2O_8$ triangular dodecahedron behaves similarly to that in andradite as the two symmetrically independent Ca–O bond distances become equal within uncertainties from about 50 to 70 GPa [Fig. 7(a)]. They start to diverge slightly again on further pressure increase to 80 GPa as shown by the excellent agreement between experiment and theory. The $Ca1O_8$ polyhedron has four symmetrically independent Ca1–O distances similar in length. On pressure increase, the Ca1–O3 bonds behave much more stiffly and hence the distortion is increased up to the spin transition, above which the distortion of the $Ca1O_8$ polyhedron is continuously decreased again [Fig. 7(b)]. The stiffness of the Ca1–O3 bonds may be explained by the O1–O3 edge sharing of the $Ca1O_8$ polyhedron with the $Ca2O_8$ polyhedron and the different compressibilities of the long Ca2–O1 and short Ca2–O3 bonds. Hence, compression is mainly compensated by the Ca–O1 bonds with respect to the Ca–O3 bonds at pressures up to about 55 GPa.

5. Hydrogen bond geometries

The hydrogen position was obtained from the theoretical data only. However, as the pressure evolutions of the theoretical interatomic distances and specifically the O · · · O distances agree very well with the experimental ones [Fig. 8(a)], we conclude that the prediction of the hydrogen position and its pressure evolution is reliable as well. At ambient conditions the interpolyhedral O3−H · · · O2 hydrogen bond has a shorter hydrogen · · · acceptor distance than the intratetrahedral O3−H · · · O3 hydrogen bonds, while the hydrogen bond angle is similar (or larger) and hence it seems to be the strongest hydrogen bond (Fig. 8). However, on pressure increase, the interpolyhedral hydrogen bond angle decreases, while the H · · · O2 distance remains nearly constant and the O3 · · · O2 distance is only slightly compressed. In contrast, the shorter of the bifurcated intratetrahedral hydrogen bonds gains in importance by a strong compression of the O3 · · · O3 and H · · · O3 distances coupled with a slight increase of the hydrogen bond angle (Fig. 8). Hence, it becomes the stronger and dominant hydrogen bond above a pressure of about 35 GPa [Fig. 8(a)]. The spin transition has only a small effect on the hydrogen bonds and does not change their relative strengths (Fig. 8).

C. Raman spectroscopy

In henritermierite of pure end-member composition there are 206 vibrational modes: $\Gamma_{\text{total}} = 14\ A_{1g} + 17\ A_{1u} + 17\ A_{2g} + 20\ A_{2u} + 15\ B_{1g} + 18\ B_{1u} + 16\ B_{2g} + 19\ B_{2u} + 38\ E_u + 32\ E_g$, of which 77 modes are Raman active: $\Gamma_{Ra} = 14\ A_{1g} + 15\ B_{1g} + 16\ B_{2g} + 32\ E_g$. The natural sample investigated in this study is of nearly end-member composition, with about 5 mole % Al on the Mn site and about 5 mole % SiO_4 tetrahedra substituting O_4H_4 tetrahedra. In the evaluation of the Raman spectra we will neglect the impurities, as it is assumed that the intensities of their Raman bands should be very weak. We have observed up to 25 Raman modes in the HS phase of henritermierite and up to 23 modes in the LS phase.

The Raman spectrum of tetragonal henritermierite at ambient conditions can be compared to the experimentally and theoretically reported Raman spectra and band assignments of stoichiometrically related cubic garnets such as andradite, $Ca_3Fe_2[SiO_4]_3$, [48–50] blythite, $Mn_3Mn_2[SiO_4]_3$, [11] and katoite, $Ca_3Al_2[O_4H_4]_3$ [51,52]. A comparison

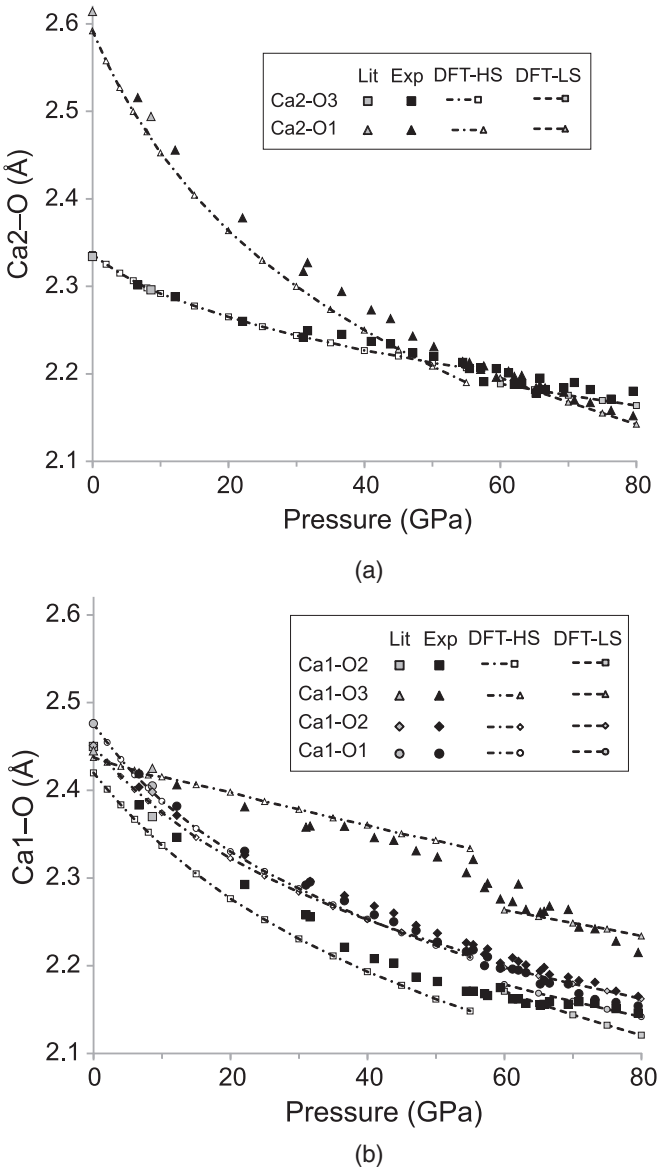

FIG. 7. Compression of the (a) Ca2–O bonds and (b) Ca1–O bonds in henritermierite obtained from experiment (Exp), literature (Lit) [8], and DFT. Lines are guides to the DFT-HS (dash-dotted lines) and DFT-LS (dashed lines) data. Errors are smaller than the symbol size.

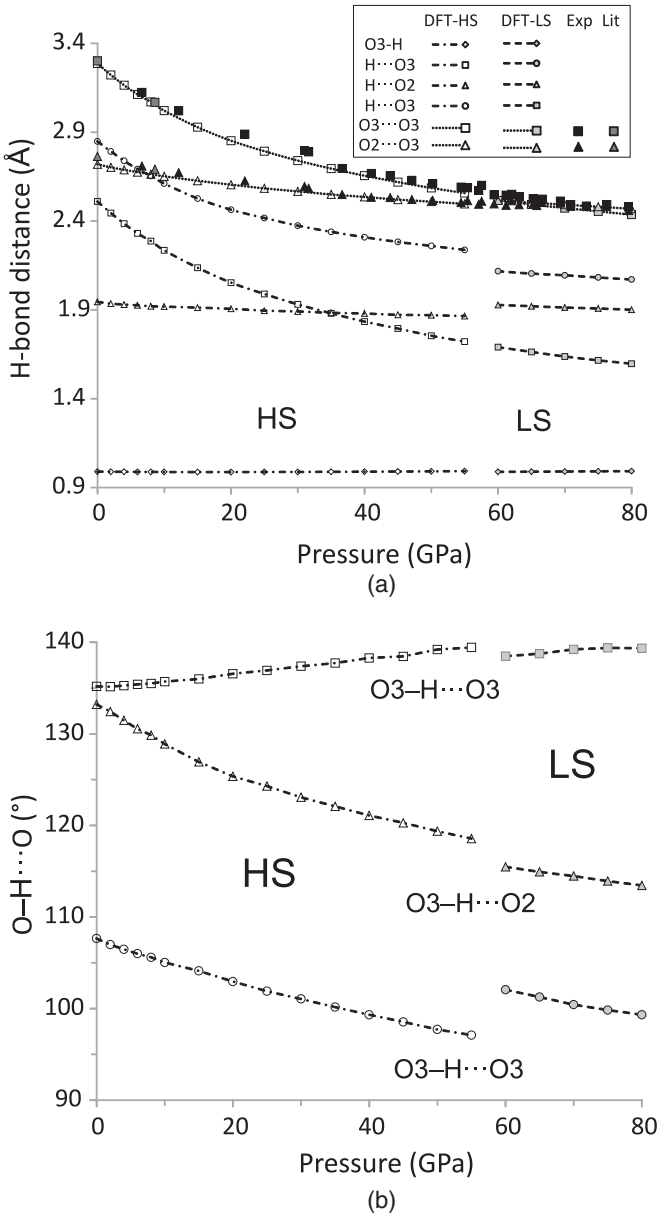

FIG. 8. Pressure evolution of the (a) hydrogen bond distances and (b) hydrogen bond angles from experiment (Exp), literature (Lit) [8], and DFT calculations for the high-spin (HS) configuration (0–55 GPa) and the low-spin (LS) configuration (60–80 GPa). Lines are guides to DFT data.

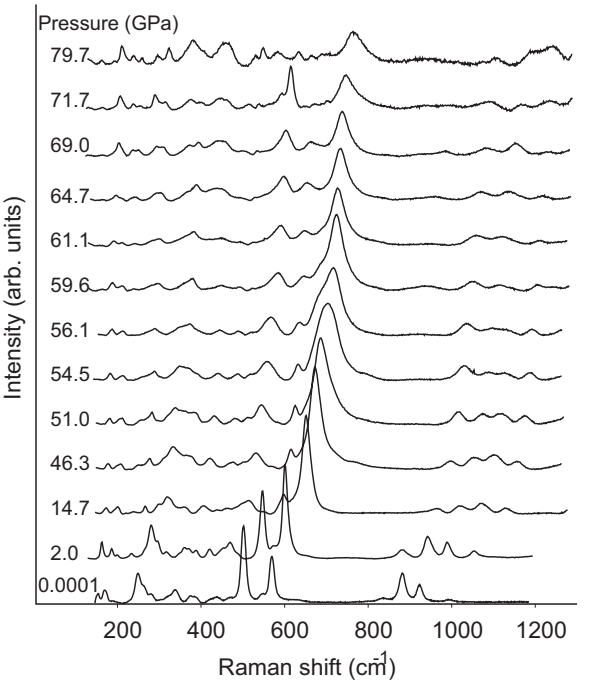

FIG. 9. Selected Raman spectra of henritermierite single crystals at high pressures and across the spin transition zone (55–70 GPa).

with the careful Raman mode assignment of andradite by Kolesov and Geiger [49] allows the assignment of the four observed high-frequency modes between 800 and 1000 cm^{-1} to Si–O stretching vibrations in henritermierite. Broad Si–O stretching modes such as those observed in blythite [11] are not detected in henritermierite at ambient conditions, which can be attributed to the ordered arrangement of the cation and $[O_4H_4]$ polyhedra in henritermierite. The low-frequency modes may be attributed to Si–O bending modes (about 400–600 cm^{-1}), R(SiO_4^{2-}) rotational modes (about 300–400 cm^{-1}), T(Ca^{2+}) translational modes (about 200–300 cm^{-1}), and T(SiO_4^{2-}) translational modes (about 150–170 cm^{-1}). Rotational and translational O_4H_4 and O–H modes may also be observed in the energy range 200–600 cm^{-1}. A broad and asymmetric Raman mode is observed at about 3428 cm^{-1} with a shoulder towards higher wave numbers, which can be attributed to O–H stretching vibrations. The frequency of the Raman mode is similar to the IR absorption mode observed in henritermierite at 3432(5) cm^{-1} [8]. This band is at rather low energy if compared to those of katoite at about 3650 cm^{-1} [51] and other hydrogarnets, as was already discussed by Armbruster *et al.* [8] for the IR absorption mode. Due to a high fluorescence background generated by the green 532-nm laser in henritermierite at above 1500 cm^{-1} and to a weak Raman signal using a red 633-nm HeNe laser, this band was not measured at high pressures. See [26] for a figure of the high-frequency O–H stretching mode. A more detailed Raman mode assignment for henritermierite requires polarized Raman spectroscopy of oriented samples and is planned for the near future within a detailed Raman spectroscopic study on different stoichiometries of manganese-containing garnets.

The pressure-induced spin crossover zone is clearly reflected in the high-pressure Raman spectra of henritermierite. While the pressure dependence of the vibrational frequencies is continuous in the HS phase, anomalies are observed between 55 and 70 GPa and indicate that the spin transition occurs gradually over a pressure range of about 15 GPa (Figs. 9 and 10). In the high-frequency range, where four Si–O stretching modes are observed in the HS phase, the overlap of two of the modes (or vanishing of one of the modes) is observed at the spin transition, while a new mode emerges at significantly lower frequency (Fig. 10). A similar behavior has also been observed in andradite at the spin transition [9]. In the LS phase an additional mode appears at about 240 cm^{-1} at 58 GPa which seems to split on further pressure increase. The Mn site does not produce Raman-active vibrations. Hence, a direct

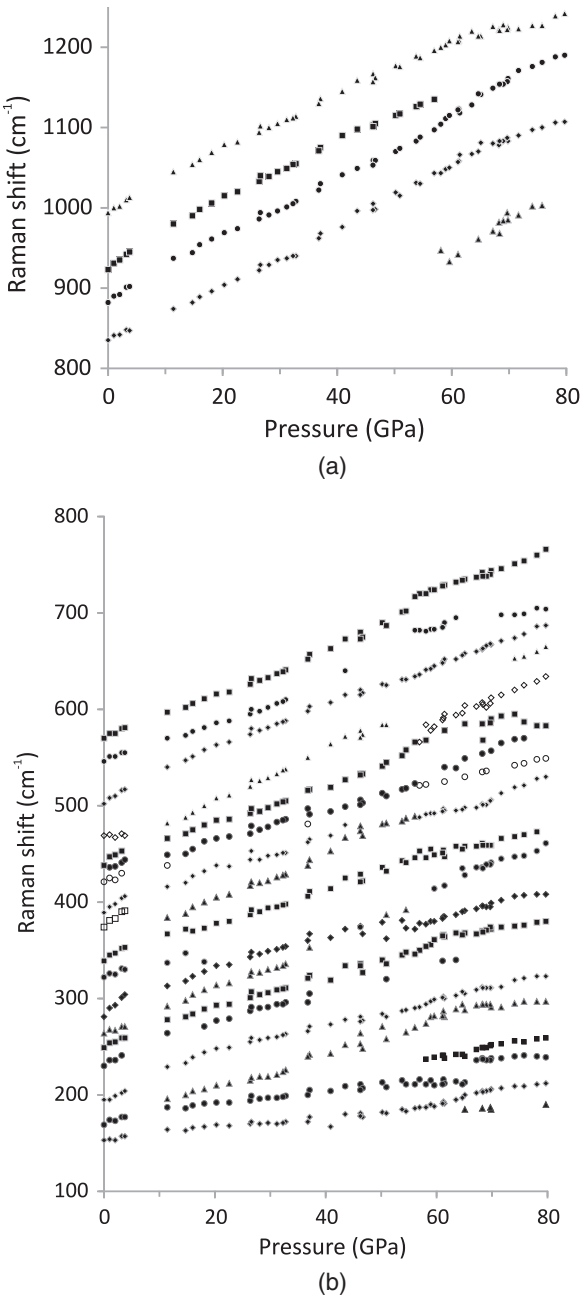

FIG. 10. Pressure-dependent shifts of the (a) high-frequency Si–O stretching modes and (b) low-frequency Raman modes of henritermierite. Anomalies and distinct changes are observed in the spin crossover region between 55 and 70 GPa.

observation of the pressure-induced spin transition from the change of the vibrations of the MnO_6 octahedra in the Raman spectra is not possible.

From the detailed pressure-dependent shifts of the Raman modes the mode Grüneisen parameters γ_i of the HS phase were calculated according to $\gamma_i = (B_0/\nu_{i0})(\partial\nu_i/\partial p)$, where B_0 is the bulk modulus at ambient pressure (GPa), ν is the frequency (cm^{-1}), p is the pressure (GPa), and ν_{i0} is the frequency of the vibrational mode i at ambient pressure (cm^{-1}), with $B_0 = 101$ GPa (Fig. 10). γ_i range between 0.34 and 0.94. Both the pressure shifts of the mode frequencies and

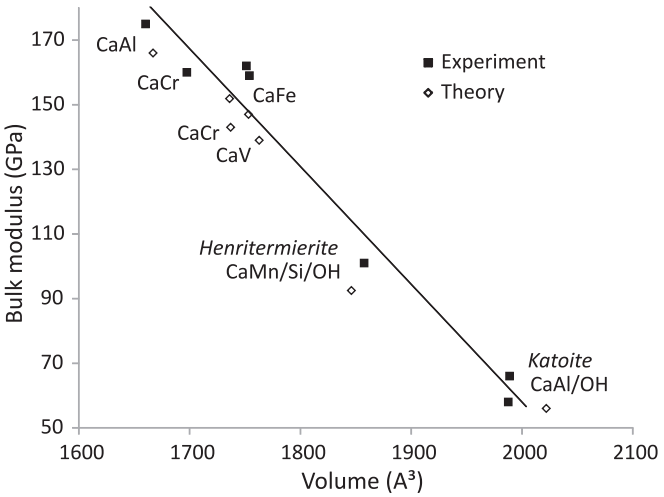

FIG. 11. Volume dependence of the bulk modulus of calcium silicate and hydro garnets. The line represents a linear fit to the experimental data. Theoretical values include literature data by Nobes *et al.* [53] for katoite, Friedrich *et al.* [9] for andradite, this study for henritermierite, and Milman *et al.* [45] for various garnet compositions. Experimental values include data by Zhang *et al.* [15], Pavese *et al.* [54] for andradite, Zhang *et al.* [15] for grossular, Diella *et al.* [55] for uvarovite, Olijnyk *et al.* [56], Lager *et al.* [13] for katoite, and this study for henritermierite.

the mode Grüneisen parameters are smaller in henritermierite compared to andradite, where γ_i range between 0.61 and 1.34 [9]. See [26] for a detailed table of the pressure-dependent shifts of the Raman modes of henritermierite and their Grüneisen parameters.

IV. DISCUSSION

A comparison of the bulk moduli of calcium silicate garnets shows an approximately linear dependence of the bulk modulus on the unit-cell volume and the large influence of the hydrogarnet substitution (Fig. 11). As was already discussed in Armbruster *et al.* [8] the bulk modulus of henritermierite is much smaller than those of OH-free silicate garnets, which generally range between 140 and 190 GPa [45]. This is attributed to the O_4H_4–SiO_4 hydrogarnet substitution. For comparison, the fully deuterated hydrogarnet katoite $Ca_3Al_2[O_4H_4]_3$ has a bulk modulus of only $B = 58(1)$ GPa [13] compared to that of grossular, $Ca_3Al_2[SiO_4]_3$ with $B = 175(1)$ GPa [15]. In our study it is shown that the volumes of the large O_4H_4 tetrahedra become similar to and even smaller than those of the small SiO_4 tetrahedra above 55 GPa (Fig. 4). This clearly shows that the hydrogarnet substitution becomes increasingly stable with increasing pressure. It is interesting to note that at the same pressure of about 55 GPa the overall structural compression mechanism changes and a pronounced reduction of the Jahn-Teller distortion is observed at higher pressure (Fig. 6), which is also interpreted as the beginning of the spin crossover zone. Although the Jahn-Teller distortion is suppressed at pressures above 70 GPa and the volumes of the O_4H_4 and SiO_4 tetrahedra are similar at >55 GPa, the symmetry of henritermierite remains tetragonal. This is due to the ordered arrangement of the O_4H_4 tetrahedra.

The pressure-induced HS-LS transition of Mn^{3+} in henritermierite occurs in a similar but slightly larger pressure range than that of Fe^{3+} in andradite, commencing at about 55 GPa (60 GPa in andradite), and is completed at about 70 GPa in both garnets (Fig. 5) [9]. However, the octahedral volume compression across the spin transition is about twice as large in andradite (about 10%) and much less gradual than in henritermierite, although the volume proportion of the FeO_6 octahedra in andradite (10%) is only slightly larger than that of the MnO_6 octahedra in henritermierite [9.4% at ambient conditions and 10.1% at 55.4(1) GPa] (Fig. 5). The smaller volume reduction in henritermierite may be explained by the smaller decrease of the Mn^{3+} ionic radius between the HS and LS state due to its $3d^4$ electronic configuration compared to that of the Fe^{3+} ion in $3d^5$ electronic configuration [57]. Further, the MnO_6 octahedron [$B_{MnO_6} = 178(2)$ GPa] in henritermierite is more compressible than the FeO_6 octahedron in andradite [$B_{FeO_6} = 195(2)$ GPa [9]]. As the polyhedral bulk modulus is one of the parameters that determine the pressure of the spin transition, this might also contribute to the lower starting pressure of the spin crossover zone in henritermierite (55 GPa) compared to that in andradite (60 GPa [9]) (Fig. 5).

V. SUMMARY AND CONCLUSION

In henritermierite we could demonstrate the complete suppression of the Jahn-Teller distortion of $Mn^{3+}O_6$ octahedra at a high pressure of 70 GPa from single-crystal structure analyses. This behavior is due to a transition from the HS state to the LS state, which is deduced from a large collapse of the octahedral volume, the absence of Jahn-Teller distortion in LS-Mn^{3+}, and the excellent agreement between experiment and theory. As the single crystals remained optically transparent and orange colored across the phase transition up to the highest pressure obtained and the Raman modes remained observable across the transition and did not vanish in the LS phase (Fig. 9), a transition to a metallic state can be excluded as the driving force for the octahedral volume collapse. This is confirmed by the DFT calculations, which indicate a significant band gap of $\approx$1.4 eV at 60 GPa in the LS state. A similar behavior was reported for andradite [9] and, hence, in both compounds the octahedral volume collapse can be attributed to the HS-LS transition and is clearly not associated with an insulator-metal transition.

The role of the hydrogen bond in spin collapse has been discussed controversially for α- and ε-FeOOH [16,17]. While in α-FeOOH a hydrogen bond symmetrization was explained to be driven by the HS-LS transition in Fe^{3+} [16], the opposite was suggested for ε-FeOOH, namely, that the HS-LS transition is driven by the hydrogen bond symmetrization [17]. In the present study, no hydrogen bond symmetrization was observed and changes in the hydrogen bond are clearly not correlated to the HS-LS transition.

Few other studies have dealt with such structural and electronic transitions in Mn^{3+} inorganic compounds. A similar concomitant suppression of the Jahn-Teller distortion of the MnF_6 octahedra and HS-LS transition in Mn^{3+} was observed in $CsMnF_3$ at 37 GPa using optical absorption spectroscopy [6]. High-pressure studies on the $A^{3+}Mn^{3+}O_3$ (A = La, Gd, Bi) compounds with distorted perovskite-type structures have shown a strong pressure-induced reduction of the Jahn-Teller distortion of $Mn^{3+}O_6$ octahedra [58–61] and the occurrence of a pressure-induced insulator-metal transition [58–60,62,63]. From the available data the authors could not resolve whether the Jahn-Teller distortion is totally suppressed at high pressure and whether this is correlated with the insulator-metal transition, and hence this was controversially discussed in both experimental and theoretical studies (e.g., [58,62–64] for $LaMnO_3$).

In summary, we conclude from our data on henritermierite that the spin transition in Mn^{3+} drives the suppression of the Jahn-Teller distortion of the MnO_6 octahedra and this mechanism is expected to occur in many other sixfold coordinated Mn^{3+}-bearing compounds as well.

ACKNOWLEDGMENTS

Financial support from the Deutsche Forschungsgemeinschaft, Germany, within priority program SPP1236 to A. Friedrich (Project No. FR-2491/2-1) and to B. Winkler (Project No. WI-1232/36); the Federal Ministry of Education and Research (BMBF), Germany (Projects No. 05KS7RF1, No. 05K10RFA, and No. 05K13RF1); and Deutsches Elektronen-Synchrotron-Photon Science, Germany is gratefully acknowledged. Portions of this research were carried out at the light source PETRA III at DESY, a member of the Helmholtz Association (HGF). We would like to thank H.-P. Liermann (PETRA III) for assistance in using beamline P02.2.

[1] W. S. Fyfe, Geochim. Cosmochim. Acta **19**, 141 (1960).
[2] M. P. Pasternak, R. D. Taylor, R. Jeanloz, X. Li, J. H. Nguyen, and C. A. McCammon, Phys. Rev. Lett. **79**, 5046 (1997).
[3] M. P. Pasternak, G. K. Rozenberg, G. Y. Machavariani, O. Naaman, R. D. Taylor, and R. Jeanloz, Phys. Rev. Lett. **82**, 4663 (1999).
[4] J. Badro, G. Fiquet, V. V. Struzhkin, M. Somayazulu, H.-k. Mao, G. Shen, and T. LeBihan, Phys. Rev. Lett. **89**, 205504 (2002).
[5] J.-P. Rueff, C.-C. Kao, V. V. Struzhkin, J. Badro, J. Shu, R. J. Hemley, and H. K. Mao, Phys. Rev. Lett. **82**, 3284 (1999).
[6] F. Aguado, F. Rodriguez, and P. Núñez, Phys. Rev. B **76**, 094417 (2007).
[7] P. A. Aubry, Y. Dusausoy, A. Laffaille, and J. Protas, Bull. Soc. fr. Minéral. Cristallogr. **92**, 126 (1969).
[8] T. Armbruster, T. Kohler, E. Libowitzky, A. Friedrich, R. Miletich, M. Kunz, O. Medenbach, and J. Gutzmer, Am. Mineral. **86**, 147 (2001).
[9] A. Friedrich, B. Winkler, W. Morgenroth, J. Ruiz-Fuertes, M. Koch-Müller, D. Rhede, and V. Milman, Phys. Rev. B **90**, 094105 (2014).
[10] H. Nishizawa and M. Koizumi, Am. Mineral. **60**, 84 (1975).
[11] T. Arlt, T. Armbruster, R. Miletich, and P. Ulmer, Phys. Chem. Minerals **26**, 100 (1998).
[12] U. Hålenius, Min. Mag. **68**, 335 (2004).

[13] G. A. Lager, R. T. Downs, M. Origlieri, and R. Garoutte, Am. Mineral. **87**, 642 (2002).

[14] G. A. Lager, W. G. Marshall, Z. Liu, and R. T. Downs, Am. Mineral. **90**, 639 (2005).

[15] L. Zhang, H. Ahsbahs, A. Kutoglu, and C. A. Geiger, Phys. Chem. Minerals **27**, 52 (1999).

[16] W. Xu, E. Greenberg, G. K. Rozenberg, M. P. Pasternak, E. Bykova, T. Boffa-Ballaran, L. Dubrovinsky, V. Prakapenka, M. Hanfland, O. Y. Vekilova, S. I. Simak, and I. A. Abrikosov, Phys. Rev. Lett. **111**, 175501 (2013).

[17] A. E. Gleason, C. E. Quiroga, A. Suzuki, R. Pentcheva, and W. L. Mao, Earth Planet. Sci. Lett. **379**, 49 (2013).

[18] H. K. Mao, J. Xu, and P. M. Bell, J. Geophys. Res. **91**, 4673 (1986).

[19] R. Boehler, Rev. Sci. Instrum. **77**, 115103 (2006).

[20] H.-P. Liermann, W. Morgenroth, A. Ehnes, A. Berghäuser, B. Winkler, H. Franz, and E. Weckert, J. Phys. Conf. Ser. **215**, 012029 (2010).

[21] A. Rothkirch, G. D. Gatta, M. Meyer, S. Merkel, M. Merlini, and H.-P. Liermann, J. Synchrotron Rad. **20**, 711 (2013).

[22] CrysAlis^{Pro} Software System, Ver. 1.171.36.28, Agilent Technologies UK, Ltd., Oxford, England, UK, 2013.

[23] G. M. Sheldrick, Acta Crystallogr. A **64**, 112 (2008).

[24] L. J. Farrugia, J. Appl. Cryst. **32**, 837 (1999).

[25] T. Balić-Zunić and I. Vickovic, J. Appl. Cryst. **29**, 305 (1996).

[26] See Supplemental Material at http://link.aps.org/supplemental/10.1103/PhysRevB.92.014117.

[27] P. A. Temple and C. E. Hathaway, Phys. Rev. B **7**, 3685 (1973).

[28] K. Syassen, DATLAB, Ver. 1.37d, MPI/FKF, Stuttgart, Germany, 2005.

[29] S. J. Clark, M. D. Segall, C. J. Pickard, P. J. Hasnip, M. J. Probert, K. Refson, and M. C. Payne, Z. Kristallogr. **220**, 567 (2005).

[30] H. J. Monkhorst and J. D. Pack, Phys. Rev. B **13**, 5188 (1976).

[31] J. P. Perdew, A. Ruzsinszky, G. I. Csonka, O. A. Vydrov, G. E. Scuseria, L. A. Constantin, X. Zhou, and K. Burke, Phys. Rev. Lett. **100**, 136406 (2008).

[32] D. A. Tompsett and M. S. Islam, Chem. Mater. **25**, 2515 (2013).

[33] G. Shao, J. Phys. Chem. C **113**, 6800 (2009).

[34] A. Elfalaky and S. Soliman, J. Alloys Compd. **580**, 401 (2013).

[35] Z. Wu, J. F. Justo, and R. M. Wentzcovitch, Phys. Rev. Lett. **110**, 228501 (2013).

[36] R. Larico, L. V. C. Assali, and J. F. Justo, Phys. Rev. B **87**, 165113 (2013).

[37] B. Siberchicot, J. Magn. Magn. Mater. **335**, 86 (2013).

[38] A. Bengtson, D. Morgan, and U. Becker, Phys. Rev. B **87**, 155141 (2013).

[39] F. Zhang and A. R. Oganov, Earth Planet. Sci. Lett. **249**, 436 (2006).

[40] H. Hsu, Y. G. Yu, and R. M. Wentzcovitch, Earth Planet. Sci. Lett. **359–360**, 34 (2012).

[41] R. Wentzcovitch, H. Hsu, and K. Umemoto, Eur. J. Mineral. **24**, 851 (2012).

[42] R. G. Burns, *Mineralogical Applications of Crystal Field Theory* (Cambridge University, Cambridge, 1993).

[43] R. J. Angel, J. Gonzalez-Platas, and M. Alvaro, Z. Kristallogr. **229**, 405 (2014).

[44] R. J. Angel, in *High-Temperature and High-Pressure Crystal Chemistry*, Rev. Mineral. Geochem. Vol. 41, edited by R. M. Hazen and R. T. Downs (Mineralogical Society of America, Geochemical Society, Chantilly, USA, 2000), pp. 35–59.

[45] V. Milman, E. V. Akhmatskaya, R. H. Nobes, B. Winkler, C. J. Pickard, and J. A. White, Acta Crystallogr. B **57**, 163 (2001).

[46] G. A. Lager and R. B. von Dreele, Am. Mineral. **81**, 1097 (1996).

[47] E. V. Akhmatskaya, R. H. Nobes, V. Milman, and B. Winkler, Z. Kristallogr. **214**, 808 (1999).

[48] A. M. Hofmeister and A. Chopelas, Phys. Chem. Minerals **17**, 503 (1991).

[49] B. A. Kolesov and C. A. Geiger, Phys. Chem. Minerals **25**, 142 (1998).

[50] F. Pascale, M. Catti, A. Damin, R. Orlando, V. R. Saunders, and R. Dovesi, J. Phys. Chem. **109**, 18522 (2005).

[51] B. A. Kolesov and C. A. Geiger, Am. Mineral. **90**, 1335 (2005).

[52] R. Orlando, F. J. Torres, F. Pascale, P. Ugliengo, C. Zicovich-Wilson, and R. Dovesi, J. Phys. Chem. B **110**, 692 (2006).

[53] R. H. Nobes, E. V. Akhmatskaya, V. Milman, J. A. White, B. Winkler, and C. J. Pickard, Am. Mineral. **85**, 1706 (2000).

[54] A. Pavese, D. Levy, and V. Pischedda, Eur. J. Mineral. **13**, 929 (2001).

[55] V. Diella, A. Sani, D. Levy, and A. Pavese, Am. Mineral. **89**, 371 (2004).

[56] H. Olijnyk, E. Paris, C. A. Geiger, and G. A. Lager, J. Geophys. Res. **96**, 14313 (1991).

[57] R. D. Shannon, Acta Crystallogr. A **32**, 751 (1976).

[58] I. Loa, P. Adler, A. Grzechnik, K. Syassen, U. Schwarz, M. Hanfland, G. K. Rozenberg, P. Gorodetsky, and M. P. Pasternak, Phys. Rev. Lett. **87**, 125501 (2001).

[59] J. Oliveira, J. Agostinho Moreira, A. Almeida, V. H. Rodrigues, M. M. R. Costa, P. B. Tavares, P. Bouvier, M. Guennou, and J. Kreisel, Phys. Rev. B **85**, 052101 (2012).

[60] M. Guennou, P. Bouvier, P. Toulemonde, C. Darie, C. Goujon, P. Bordet, M. Hanfland, and J. Kreisel, Phys. Rev. Lett. **112**, 075501 (2014).

[61] G. Calestani, F. Orlandi, F. Mezzadri, L. Righi, M. Merlini, and E. Gilioli, Inorg. Chem. **53**, 8749 (2014).

[62] M. Baldini, V. V. Struzhkin, A. F. Goncharov, P. Postorino, and W. L. Mao, Phys. Rev. Lett. **106**, 066402 (2011).

[63] A. Y. Ramos, N. M. Souza-Neto, H. C. N. Tolentino, O. Bunau, Y. Joly, S. Grenier, J.-P. Itié, A.-M. Flank, P. Lagarde, and A. Caneiro, Eur. Phys. Lett. **96**, 36002 (2011).

[64] J. He, M.-X. Chen, X.-Q. Chen, and C. Franchini, Phys. Rev. B **85**, 195135 (2012).